# Compressed sensing for radio interferometric imaging on wide fields of view

Jason McEwen
http://lts2www.epfl.ch/~mcewen/

*BASP research node*

*Institute of Electrical Engineering,*
*Ecole Polytechnique Fédérale de Lausanne (EPFL), Switzerland*

CALIM 2010 :: Dwingeloo, Netherlands

# Outline

# Radio interferometry

- The complex visibility measured by an interferometer is given by the coordinate free definition

$$\mathcal{V}(\boldsymbol{b}_{\boldsymbol{\lambda}}) = \int_{\mathrm{S}^2} A(\boldsymbol{\sigma}) I(\boldsymbol{\sigma}) \mathrm{e}^{-\mathrm{i}2\pi \boldsymbol{b}_{\boldsymbol{\lambda}} \cdot \boldsymbol{\sigma}} \, \mathrm{d}\Omega \, .$$

- Expressed in the usual local coordinate system

$$y(\boldsymbol{u}, w) = \int_{D^2} A(\boldsymbol{l}) \, x_{\mathrm{p}}(\boldsymbol{l}) \, \mathrm{e}^{-\mathrm{i}2\pi [\boldsymbol{u}\cdot \boldsymbol{l} + w\,(n(\boldsymbol{l})-1)]} \, \frac{\mathrm{d}^2 \boldsymbol{l}}{n(\boldsymbol{l})}$$
$$= \int_{D^2} A(\boldsymbol{l}) \, x_{\mathrm{p}}(\boldsymbol{l}) \, C^{(w)}(\|\boldsymbol{l}\|) \, \mathrm{e}^{-\mathrm{i}2\pi \boldsymbol{u}\cdot \boldsymbol{l}} \, \frac{\mathrm{d}^2 \boldsymbol{l}}{n(\boldsymbol{l})} \, ,$$

where $\boldsymbol{l} = (l, m)$, $\|\boldsymbol{l}\|^2 + n^2(\boldsymbol{l}) = 1$ and the chirp $C^{(w)}(\|\boldsymbol{l}\|)$ is given by

$$C^{(w)}(\|\boldsymbol{l}\|) \equiv \mathrm{e}^{\mathrm{i}2\pi w \left(1 - \sqrt{1 - \|\boldsymbol{l}\|^2}\right)} \, .$$

- Typically small field-of-view (FOV) assumptions are made with $\mathrm{d}\Omega = \mathrm{d}^2\boldsymbol{l}/n(\boldsymbol{l}) \simeq \mathrm{d}^2\boldsymbol{l}$ and
  - $\|\boldsymbol{l}\|^2 w \ll 1 \quad \Rightarrow \quad C^{(w)}(\|\boldsymbol{l}\|) \simeq 1$
  - $\|\boldsymbol{l}\|^4 w \ll 1 \quad \Rightarrow \quad C^{(w)}(\|\boldsymbol{l}\|) \simeq \mathrm{e}^{\mathrm{i}\pi w \|\boldsymbol{l}\|^2}$ (Wiaux *et al.* 2009 [6])

# Radio interferometry

- The complex visibility measured by an interferometer is given by the coordinate free definition

$$\mathcal{V}(\boldsymbol{b}_{\boldsymbol{\lambda}}) = \int_{S^2} A(\boldsymbol{\sigma}) I(\boldsymbol{\sigma}) \mathrm{e}^{-\mathrm{i}2\pi \boldsymbol{b}_{\boldsymbol{\lambda}} \cdot \boldsymbol{\sigma}} \, \mathrm{d}\Omega \, .$$

- Expressed in the usual local coordinate system

$$\begin{aligned} y(\boldsymbol{u}, w) &= \int_{D^2} A(\boldsymbol{l}) \, x_{\mathrm{p}}(\boldsymbol{l}) \, \mathrm{e}^{-\mathrm{i}2\pi [\boldsymbol{u} \cdot \boldsymbol{l} + w \, (n(\boldsymbol{l}) - 1)]} \, \frac{\mathrm{d}^2 \boldsymbol{l}}{n(\boldsymbol{l})} \\ &= \int_{D^2} A(\boldsymbol{l}) \, x_{\mathrm{p}}(\boldsymbol{l}) \, C^{(w)}(\|\boldsymbol{l}\|) \, \mathrm{e}^{-\mathrm{i}2\pi \boldsymbol{u} \cdot \boldsymbol{l}} \, \frac{\mathrm{d}^2 \boldsymbol{l}}{n(\boldsymbol{l})} \, , \end{aligned}$$

where $\boldsymbol{l} = (l, m)$, $\|\boldsymbol{l}\|^2 + n^2(\boldsymbol{l}) = 1$ and the chirp $C^{(w)}(\|\boldsymbol{l}\|)$ is given by

$$C^{(w)}(\|\boldsymbol{l}\|) \equiv \mathrm{e}^{\mathrm{i}2\pi w \left(1 - \sqrt{1 - \|\boldsymbol{l}\|^2}\right)} \, .$$

- Typically small field-of-view (FOV) assumptions are made with $\mathrm{d}\Omega = \mathrm{d}^2\boldsymbol{l}/n(\boldsymbol{l}) \simeq \mathrm{d}^2\boldsymbol{l}$ and
  - $\|\boldsymbol{l}\|^2 w \ll 1 \quad \Rightarrow \quad C^{(w)}(\|\boldsymbol{l}\|) \simeq 1$
  - $\|\boldsymbol{l}\|^4 w \ll 1 \quad \Rightarrow \quad C^{(w)}(\|\boldsymbol{l}\|) \simeq \mathrm{e}^{\mathrm{i}\pi w \|\boldsymbol{l}\|^2}$ (Wiaux *et al.* 2009 [6])

# Radio interferometry

- The complex visibility measured by an interferometer is given by the coordinate free definition

$$\mathcal{V}(\boldsymbol{b}_{\boldsymbol{\lambda}}) = \int_{\mathrm{S}^2} A(\boldsymbol{\sigma}) I(\boldsymbol{\sigma}) \mathrm{e}^{-\mathrm{i}2\pi \boldsymbol{b}_{\boldsymbol{\lambda}} \cdot \boldsymbol{\sigma}} \, \mathrm{d}\Omega \, .$$

- Expressed in the usual local coordinate system

$$y(\boldsymbol{u}, w) = \int_{D^2} A(\boldsymbol{l}) \, x_{\mathrm{p}}(\boldsymbol{l}) \, \mathrm{e}^{-\mathrm{i}2\pi [\boldsymbol{u} \cdot \boldsymbol{l} + w\,(n(\boldsymbol{l})-1)]} \, \frac{\mathrm{d}^2 \boldsymbol{l}}{n(\boldsymbol{l})}$$

$$= \int_{D^2} A(\boldsymbol{l}) \, x_{\mathrm{p}}(\boldsymbol{l}) \, C^{(w)}(\|\boldsymbol{l}\|) \, \mathrm{e}^{-\mathrm{i}2\pi \boldsymbol{u} \cdot \boldsymbol{l}} \, \frac{\mathrm{d}^2 \boldsymbol{l}}{n(\boldsymbol{l})} \, ,$$

where $\boldsymbol{l} = (l, m)$, $\|\boldsymbol{l}\|^2 + n^2(\boldsymbol{l}) = 1$ and the chirp $C^{(w)}(\|\boldsymbol{l}\|)$ is given by

$$C^{(w)}(\|\boldsymbol{l}\|) \equiv \mathrm{e}^{\mathrm{i}2\pi w \left(1 - \sqrt{1 - \|\boldsymbol{l}\|^2}\right)} \, .$$

- Typically small field-of-view (FOV) assumptions are made with $\mathrm{d}\Omega = \mathrm{d}^2\boldsymbol{l}/n(\boldsymbol{l}) \simeq \mathrm{d}^2\boldsymbol{l}$ and
  - $\|\boldsymbol{l}\|^2 \, w \ll 1 \quad \Rightarrow \quad C^{(w)}(\|\boldsymbol{l}\|) \simeq 1$
  - $\|\boldsymbol{l}\|^4 \, w \ll 1 \quad \Rightarrow \quad C^{(w)}(\|\boldsymbol{l}\|) \simeq \mathrm{e}^{\mathrm{i}\pi w \|\boldsymbol{l}\|^2}$ (Wiaux *et al.* 2009 [6])

# Spread spectrum phenomenon

- Modulation by the chirp spreads the spectrum of the signal.
- Recall that for Fourier measurements the compressed sensing (CS) coherence is the maximum modulus of the Fourier transform on the sparsity basis vectors: $\mu = \max_{i,j} |\boldsymbol{f}_i \cdot \psi_j|$.
- Consequently, spreading the spectrum increases the incoherence between the sensing and sparsity bases, thus improving the performance of CS reconstructions.

- When no small-field assumption is made the chirp modulation contains higher frequency content $\Rightarrow$ improved effectiveness of chirp on wide FOV.

# Spread spectrum phenomenon

- Modulation by the chirp spreads the spectrum of the signal.
- Recall that for Fourier measurements the compressed sensing (CS) coherence is the maximum modulus of the Fourier transform on the sparsity basis vectors: $\mu = \max_{i,j} |\boldsymbol{f}_i \cdot \psi_j|$.
- Consequently, spreading the spectrum increases the incoherence between the sensing and sparsity bases, thus improving the performance of CS reconstructions.

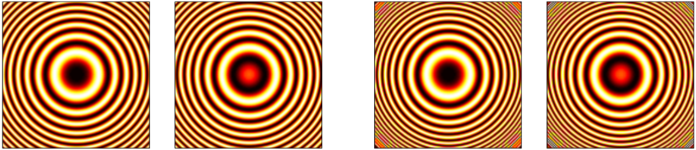

(a) Assuming $\|\boldsymbol{l}\|^4 \, w \ll 1$ (b) No small-field assumption

Figure: Real part and imaginary part of chirp modulation for FOV $\theta_{\mathrm{FOV}} = 90^\circ$.

- When no small-field assumption is made the chirp modulation contains higher frequency content $\Rightarrow$ improved effectiveness of chirp on wide FOV.

# Band-limited signals

- Consider signal on the sphere and project onto tangent plane defined by usual $\boldsymbol{l} = (l, m)$ coordinates.
- Ensure a band-limited signal on the sphere is sufficiently sampled on plane when projected.
- Band-limit relations between the sphere and plane:
  - Small FOV: $L \simeq 2\pi B$
  - Wide FOV: $L_{\text{FOV}} \simeq 2\pi \cos(\theta_{\text{FOV}}/2) B_{\text{FOV}}$

  where $L$ and $B$ are band-limits on the sphere and plane respectively.
- Band-limit relations define sampling resolutions.
- Adopt `HEALPix` pixelisation of the sphere [2].
- For wide FOV $N_{\text{p}}/N_{\text{s}}$ increases rapidly
  $\Rightarrow$ signal less sparse on plane;
  $\Rightarrow$ superiority of sphere.

# Band-limited signals

- Consider signal on the sphere and project onto tangent plane defined by usual $\boldsymbol{l} = (l, m)$ coordinates.
- Ensure a band-limited signal on the sphere is sufficiently sampled on plane when projected.
- Band-limit relations between the sphere and plane:
  - Small FOV: $L \simeq 2\pi B$
  - Wide FOV: $L_{\mathrm{FOV}} \simeq 2\pi \cos(\theta_{\mathrm{FOV}}/2) B_{\mathrm{FOV}}$

  where $L$ and $B$ are band-limits on the sphere and plane respectively.
- Band-limit relations define sampling resolutions.
- Adopt HEALPix pixelisation of the sphere [2].
- For wide FOV $N_{\mathrm{p}}/N_{\mathrm{s}}$ increases rapidly
  $\Rightarrow$ signal less sparse on plane;
  $\Rightarrow$ superiority of sphere.

# Band-limited signals

- Consider signal on the sphere and project onto tangent plane defined by usual $\boldsymbol{l} = (l, m)$ coordinates.
- Ensure a band-limited signal on the sphere is sufficiently sampled on plane when projected.
- Band-limit relations between the sphere and plane:
  - Small FOV: $L \simeq 2\pi B$
  - Wide FOV: $L_{\rm FOV} \simeq 2\pi \cos(\theta_{\rm FOV}/2) B_{\rm FOV}$

  where $L$ and $B$ are band-limits on the sphere and plane respectively.
- Band-limit relations define sampling resolutions.
- Adopt HEALPix pixelisation of the sphere [2].
- For wide FOV $N_{\rm p}/N_{\rm s}$ increases rapidly
  $\Rightarrow$ signal less sparse on plane;
  $\Rightarrow$ superiority of sphere.

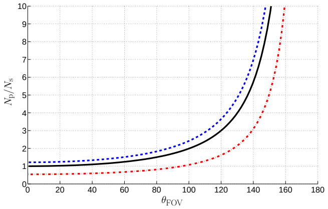


Figure: Ratio of number of samples on the plane to the sphere ($N_{\rm p}/N_{\rm s}$). Plotted for $L = cN_{\rm side}$, with $c = 3$ (blue); $c = \sqrt{3}\,\pi/2$ (black); $c = 2$ (red).

# Band-limited signals

- Consider signal on the sphere and project onto tangent plane defined by usual $\boldsymbol{l} = (l, m)$ coordinates.
- Ensure a band-limited signal on the sphere is sufficiently sampled on plane when projected.
- Band-limit relations between the sphere and plane:
  - Small FOV: $L \simeq 2\pi B$
  - Wide FOV: $L_{\text{FOV}} \simeq 2\pi \cos(\theta_{\text{FOV}}/2) B_{\text{FOV}}$

  where $L$ and $B$ are band-limits on the sphere and plane respectively.
- Band-limit relations define sampling resolutions.
- Adopt HEALPix pixelisation of the sphere [2].
- For wide FOV $N_{\text{p}}/N_{\text{s}}$ increases rapidly
  $\Rightarrow$ signal less sparse on plane;
  $\Rightarrow$ superiority of sphere.

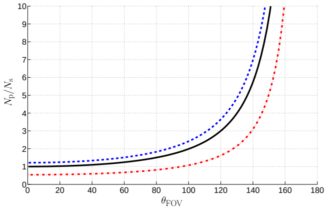


Figure: Ratio of number of samples on the plane to the sphere ($N_{\text{p}}/N_{\text{s}}$). Plotted for $L = cN_{\text{side}}$, with $c = 3$ (blue); $c = \sqrt{3}\,\pi/2$ (black); $c = 2$ (red).

# Projection operators

- Project onto a regular grid on the plane to reduce significantly the computational load of subsequent analyses through the use of FFTs.
- Regridding operation is required $\longrightarrow$ convolutional gridding (*cf.* regridding performed when mapping the visibilities observed at continuous coordinates to a regular grid, also to afford the use of FFTs).
- Consider box, Gaussian and sinc kernels.
- Select Gaussian kernel due to space-frequency trade-off (other kernels could also be considered, *e.g.* Gaussian-sinc, spheriodal functions).
- Incoherence reduced on sphere due to projection P:

$$\mu_{\rm s} = \max_{i,j} |f_i \cdot \mathsf{P}\psi_j| ,$$

$\Rightarrow$ hampers CS reconstruction performance;

$\Rightarrow$ employ universality of chirp.

# Projection operators

- Project onto a regular grid on the plane to reduce significantly the computational load of subsequent analyses through the use of FFTs.
- Regridding operation is required → convolutional gridding (*cf.* regridding performed when mapping the visibilities observed at continuous coordinates to a regular grid, also to afford the use of FFTs).
- Consider box, Gaussian and sinc kernels.
- Select Gaussian kernel due to space-frequency trade-off (other kernels could also be considered, *e.g.* Gaussian-sinc, spheriodal functions).
- Incoherence reduced on sphere due to projection P:

$$\mu_s = \max_{i,j} |f_i \cdot \mathrm{P}\psi_j| ,$$

⇒ hampers CS reconstruction performance;

⇒ employ universality of chirp.

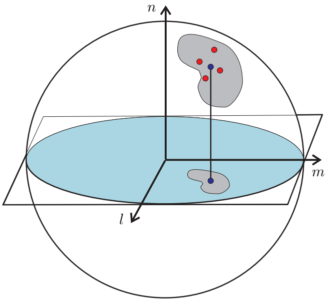


Figure: Projection of a sampled signal from the sphere to the plane.

# Projection operators

- Project onto a regular grid on the plane to reduce significantly the computational load of subsequent analyses through the use of FFTs.
- Regridding operation is required → convolutional gridding (*cf.* regridding performed when mapping the visibilities observed at continuous coordinates to a regular grid, also to afford the use of FFTs).
- Consider box, Gaussian and sinc kernels.
- Select Gaussian kernel due to space-frequency trade-off (other kernels could also be considered, *e.g.* Gaussian-sinc, spheriodal functions).
- Incoherence reduced on sphere due to projection P:

$$\mu_s = \max_{i,j} |\boldsymbol{f}_i \cdot \mathrm{P}\psi_j|,$$

⇒ hampers CS reconstruction performance;

⇒ employ universality of chirp.

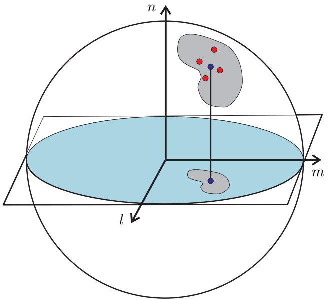


Figure: Projection of a sampled signal from the sphere to the plane.

# Projection operators

- Project onto a regular grid on the plane to reduce significantly the computational load of subsequent analyses through the use of FFTs.
- Regridding operation is required $\longrightarrow$ convolutional gridding (*cf.* regridding performed when mapping the visibilities observed at continuous coordinates to a regular grid, also to afford the use of FFTs).
- Consider box, Gaussian and sinc kernels.
- Select Gaussian kernel due to space-frequency trade-off (other kernels could also be considered, *e.g.* Gaussian-sinc, spheriodal functions).
- Incoherence reduced on sphere due to projection P:

$$\mu_{\rm s} = \max_{i,j} |\boldsymbol{f}_i \cdot \mathsf{P}\psi_j|,$$

$\Rightarrow$ hampers CS reconstruction performance;

$\Rightarrow$ employ universality of chirp.

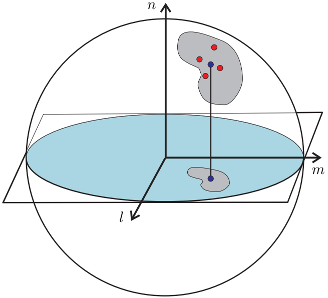


Figure: Projection of a sampled signal from the sphere to the plane.

# Interferometric inverse problem

- Ill-posed interferometric inverse problem:

$$\boldsymbol{y} = \Phi_m^{(w)} \boldsymbol{x}_m + \boldsymbol{n},$$

where $m = \{\mathrm{s}, \mathrm{p}\}$,

$$\Phi_\mathrm{p}^{(w)} = \mathsf{W\,M\,F\,C}^{(w)}\,\mathsf{A}$$

and

$$\Phi_\mathrm{s}^{(w)} = \mathsf{W\,M\,F\,C}^{(w)}\,\mathsf{A\,G\,P}.$$

- Consider reconstruction problems on the sphere and plane.
  - BP reconstruction with Dirac sparsity basis:

$$\min_{\boldsymbol{x}_m} \|\boldsymbol{x}_m\|_1 \text{ such that } \|\boldsymbol{y} - \Phi_m^{(w)} \boldsymbol{x}_m\|_2 \leq \epsilon$$

  - TV reconstruction:

$$\min_{\boldsymbol{x}_m} \|\boldsymbol{x}_m\|_{\mathrm{TV}} \text{ such that } \|\boldsymbol{y} - \Phi_m^{(w)} \boldsymbol{x}_m\|_2 \leq \epsilon$$

# Interferometric inverse problem

- Ill-posed interferometric inverse problem:

$$\boldsymbol{y} = \Phi_m^{(w)} \boldsymbol{x}_m + \boldsymbol{n},$$

  where $m = \{\mathrm{s}, \mathrm{p}\}$,

$$\Phi_\mathrm{p}^{(w)} = \mathsf{W}\,\mathsf{M}\,\mathsf{F}\,\mathsf{C}^{(w)}\,\mathsf{A}$$

  and

$$\Phi_\mathrm{s}^{(w)} = \mathsf{W}\,\mathsf{M}\,\mathsf{F}\,\mathsf{C}^{(w)}\,\mathsf{A}\,\mathsf{G}\,\mathsf{P}.$$

- Consider reconstruction problems on the sphere and plane.
  - BP reconstruction with Dirac sparsity basis:

$$\min_{\boldsymbol{x}_m} \|\boldsymbol{x}_m\|_1 \text{ such that } \|\boldsymbol{y} - \Phi_m^{(w)} \boldsymbol{x}_m\|_2 \leq \epsilon$$

  - TV reconstruction:

$$\min_{\boldsymbol{x}_m} \|\boldsymbol{x}_m\|_{\mathrm{TV}} \text{ such that } \|\boldsymbol{y} - \Phi_m^{(w)} \boldsymbol{x}_m\|_2 \leq \epsilon$$

# Reconstruction of simulated Gaussian maps

- Quantify performance on simulations of Gaussians of various sizes: $\sigma_S = \{0.01, 0.02, 0.04, 0.10\}$.
- Consider $\theta_{\rm FOV} = 90^\circ$ and $N_{\rm side} = 32$ $\Rightarrow L_{\rm FOV} \simeq 90$; $N_s \simeq 1740$; $B_{\rm FOV} \simeq 20$; $N_p \simeq 3360$.
- Beam $\rm FWHM = 45^\circ$.
- Chirp $w_d = \{0, 1/\sqrt{2}\}$ (corresponding to continuous $w \simeq \{0, B_{\rm FOV}\}$).

# Reconstruction of simulated Gaussian maps

- Quantify performance on simulations of Gaussians of various sizes: $\sigma_S = \{0.01, 0.02, 0.04, 0.10\}$.
- Consider $\theta_{FOV} = 90^\circ$ and $N_{side} = 32$ $\Rightarrow L_{FOV} \simeq 90$; $N_s \simeq 1740$; $B_{FOV} \simeq 20$; $N_p \simeq 3360$.
- Beam FWHM $= 45^\circ$.
- Chirp $w_d = \{0, 1/\sqrt{2}\}$ (corresponding to continuous $w \simeq \{0, B_{FOV}\}$).

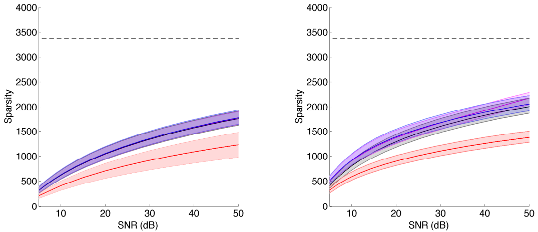


(a) Dirac sparsity for $\sigma_S = 0.10$ (b) TV sparsity for $\sigma_S = 0.10$

Figure: Sparsities on the sphere (red) and plane for various projection operators (other colours).

ÉCOLE POLYTECHNIQUE FÉDÉRALE DE LAUSANNE

# Reconstruction of simulated Gaussian maps

- Quantify performance on simulations of Gaussians of various sizes: $\sigma_S = \{0.01, 0.02, 0.04, 0.10\}$.
- Consider $\theta_{FOV} = 90^\circ$ and $N_{side} = 32$ $\Rightarrow L_{FOV} \simeq 90$; $N_s \simeq 1740$; $B_{FOV} \simeq 20$; $N_p \simeq 3360$.
- Beam FWHM $= 45^\circ$.
- Chirp $w_d = \{0, 1/\sqrt{2}\}$ (corresponding to continuous $w \simeq \{0, B_{FOV}\}$).

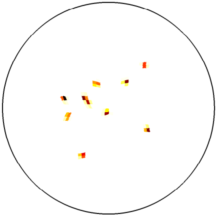

(a) Spherical image

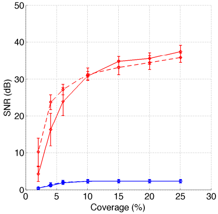


(b) $\text{SNR}_s$ for BP

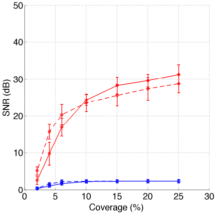


(c) $\text{SNR}_s$ for TV

Figure: Reconstruction performance for $\sigma_S = 0.01$ (blue – plane; red – sphere; solid – no chirp; dashed – with chirp).

# Reconstruction of simulated Gaussian maps

- Quantify performance on simulations of Gaussians of various sizes: $\sigma_{\text{S}} = \{0.01, 0.02, 0.04, 0.10\}$.
- Consider $\theta_{\text{FOV}} = 90^\circ$ and $N_{\text{side}} = 32$ $\Rightarrow L_{\text{FOV}} \simeq 90$; $N_{\text{s}} \simeq 1740$; $B_{\text{FOV}} \simeq 20$; $N_{\text{p}} \simeq 3360$.
- Beam FWHM $= 45^\circ$.
- Chirp $w_{\text{d}} = \{0, 1/\sqrt{2}\}$ (corresponding to continuous $w \simeq \{0, B_{\text{FOV}}\}$).

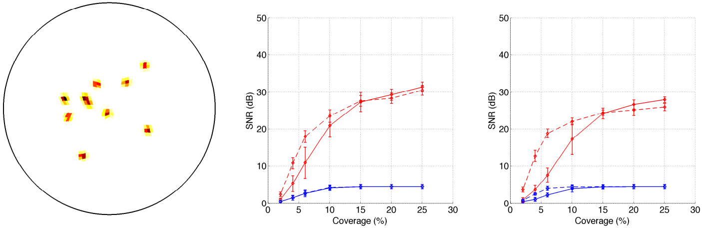


(a) Spherical image (b) $\text{SNR}_{\text{s}}$ for BP (c) $\text{SNR}_{\text{s}}$ for TV

Figure: Reconstruction performance for $\sigma_{\text{S}} = 0.02$ (blue – plane; red – sphere; solid – no chirp; dashed – with chirp).

# Reconstruction of simulated Gaussian maps

- Quantify performance on simulations of Gaussians of various sizes: $\sigma_S = \{0.01, 0.02, 0.04, 0.10\}$.
- Consider $\theta_{FOV} = 90^\circ$ and $N_{side} = 32$ $\Rightarrow L_{FOV} \simeq 90$; $N_s \simeq 1740$; $B_{FOV} \simeq 20$; $N_p \simeq 3360$.
- Beam $\mathrm{FWHM} = 45^\circ$.
- Chirp $w_d = \{0, 1/\sqrt{2}\}$ (corresponding to continuous $w \simeq \{0, B_{FOV}\}$).

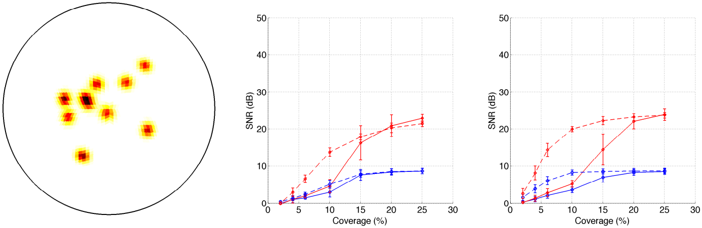


(a) Spherical image (b) $\mathrm{SNR_s}$ for BP (c) $\mathrm{SNR_s}$ for TV

Figure: Reconstruction performance for $\sigma_S = 0.04$ (blue – plane; red – sphere; solid – no chirp; dashed – with chirp).

# Reconstruction of simulated Gaussian maps

- Quantify performance on simulations of Gaussians of various sizes: $\sigma_{\mathrm{S}} = \{0.01, 0.02, 0.04, 0.10\}$.
- Consider $\theta_{\mathrm{FOV}} = 90^\circ$ and $N_{\mathrm{side}} = 32$ $\Rightarrow L_{\mathrm{FOV}} \simeq 90; N_{\mathrm{s}} \simeq 1740; B_{\mathrm{FOV}} \simeq 20; N_{\mathrm{p}} \simeq 3360.$
- Beam FWHM $= 45^\circ$.
- Chirp $w_{\mathrm{d}} = \{0, 1/\sqrt{2}\}$ (corresponding to continuous $w \simeq \{0, B_{\mathrm{FOV}}\}$).

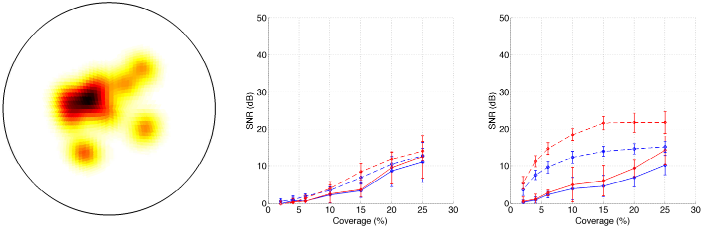


(a) Spherical image (b) $\mathrm{SNR_s}$ for BP (c) $\mathrm{SNR_s}$ for TV

Figure: Reconstruction performance for $\sigma_{\mathrm{S}} = 0.10$ (blue – plane; red – sphere; solid – no chirp; dashed – with chirp).

# Reconstruction of simulated Gaussian maps

- Quantify performance on simulations of Gaussians of various sizes: $\sigma_S = \{0.01, 0.02, 0.04, 0.10\}$.
- Consider $\theta_{FOV} = 90^\circ$ and $N_{side} = 32$
  $\Rightarrow L_{FOV} \simeq 90; N_s \simeq 1740; B_{FOV} \simeq 20; N_p \simeq 3360$.
- Beam FWHM $= 45^\circ$.
- Chirp $w_d = \{0, 1/\sqrt{2}\}$ (corresponding to continuous $w \simeq \{0, B_{FOV}\}$).

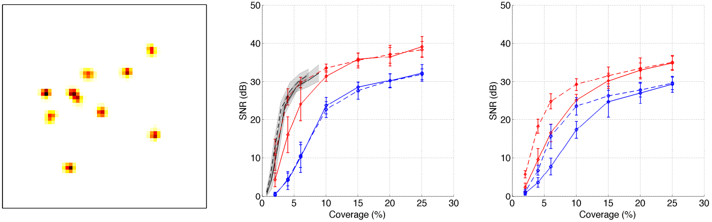


(a) Planar image (b) $\text{SNR}_p$ for BP (c) $\text{SNR}_p$ for TV

Figure: Reconstruction performance for $\sigma_S = 0.01$ (blue – plane; red – sphere; solid – no chirp; dashed –with chirp).

# Reconstruction of simulated Gaussian maps

- Quantify performance on simulations of Gaussians of various sizes: $\sigma_{\rm S} = \{0.01, 0.02, 0.04, 0.10\}$.
- Consider $\theta_{\rm FOV} = 90^\circ$ and $N_{\rm side} = 32$ $\Rightarrow L_{\rm FOV} \simeq 90$; $N_{\rm s} \simeq 1740$; $B_{\rm FOV} \simeq 20$; $N_{\rm p} \simeq 3360$.
- Beam FWHM $= 45^\circ$.
- Chirp $w_{\rm d} = \{0, 1/\sqrt{2}\}$ (corresponding to continuous $w \simeq \{0, B_{\rm FOV}\}$).

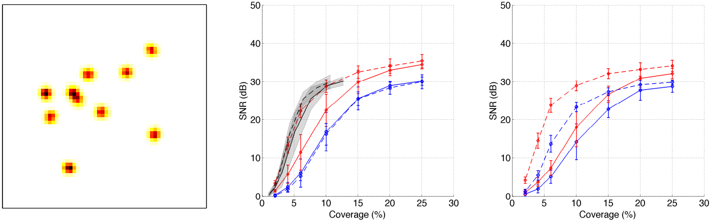


(a) Planar image (b) $\mathrm{SNR_p}$ for BP (c) $\mathrm{SNR_p}$ for TV

Figure: Reconstruction performance for $\sigma_{\rm S} = 0.02$ (blue – plane; red – sphere; solid – no chirp; dashed –with chirp).

# Reconstruction of simulated Gaussian maps

- Quantify performance on simulations of Gaussians of various sizes: $\sigma_S = \{0.01, 0.02, 0.04, 0.10\}$.
- Consider $\theta_{\mathrm{FOV}} = 90^\circ$ and $N_{\mathrm{side}} = 32$ $\Rightarrow L_{\mathrm{FOV}} \simeq 90; N_s \simeq 1740; B_{\mathrm{FOV}} \simeq 20; N_p \simeq 3360.$
- Beam FWHM $= 45^\circ$.
- Chirp $w_d = \{0, 1/\sqrt{2}\}$ (corresponding to continuous $w \simeq \{0, B_{\mathrm{FOV}}\}$).

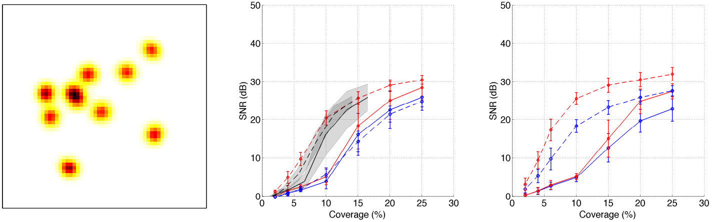


(a) Planar image | (b) $\mathrm{SNR_p}$ for BP | (c) $\mathrm{SNR_p}$ for TV

Figure: Reconstruction performance for $\sigma_S = 0.04$ (blue – plane; red – sphere; solid – no chirp; dashed –with chirp).

# Reconstruction of simulated Gaussian maps

- Quantify performance on simulations of Gaussians of various sizes: $\sigma_S = \{0.01, 0.02, 0.04, 0.10\}$.
- Consider $\theta_{\text{FOV}} = 90^\circ$ and $N_{\text{side}} = 32$ $\Rightarrow L_{\text{FOV}} \simeq 90$; $N_s \simeq 1740$; $B_{\text{FOV}} \simeq 20$; $N_p \simeq 3360$.
- Beam FWHM $= 45^\circ$.
- Chirp $w_d = \{0, 1/\sqrt{2}\}$ (corresponding to continuous $w \simeq \{0, B_{\text{FOV}}\}$).

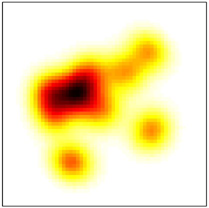

(a) Planar image

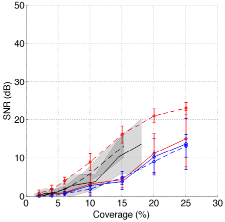


(b) $\text{SNR}_p$ for BP

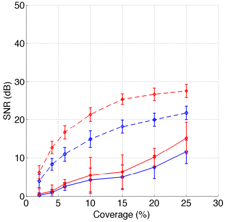


(c) $\text{SNR}_p$ for TV

Figure: Reconstruction performance for $\sigma_S = 0.10$ (blue – plane; red – sphere; solid – no chirp; dashed –with chirp).

# Reconstruction of Galactic dust map

- Consider more realistic simulation of 94GHz FDS map of predicted submillimeter and microwave emission of diffuse interstellar Galactic dust [1]
  (available form LAMBDA website: `http://lambda.gsfc.nasa.gov`).
- Downsample to resolution of $N_{\rm side} = 128$ and consider region of $\theta_{\rm FOV} = 90^\circ$ centered on Galactic coordinates $(l, b) = (210^\circ, -20^\circ)$.
- Reconstruct from simulated visibilities with 25% coverage.

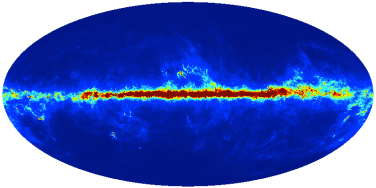

(a) Mollweide projection of full-sky

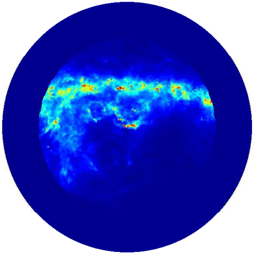

(b) Orthographic projection of FOV

Figure: FDS map of predicted emission of diffuse interstellar Galactic dust.

# Reconstruction of Galactic dust map

- Consider more realistic simulation of 94GHz FDS map of predicted submillimeter and microwave emission of diffuse interstellar Galactic dust [1]
  (available form LAMBDA website: `http://lambda.gsfc.nasa.gov`).
- Downsample to resolution of $N_{\text{side}} = 128$ and consider region of $\theta_{\text{FOV}} = 90^\circ$ centered on Galactic coordinates $(l, b) = (210^\circ, -20^\circ)$.
- Reconstruct from simulated visibilities with 25% coverage.

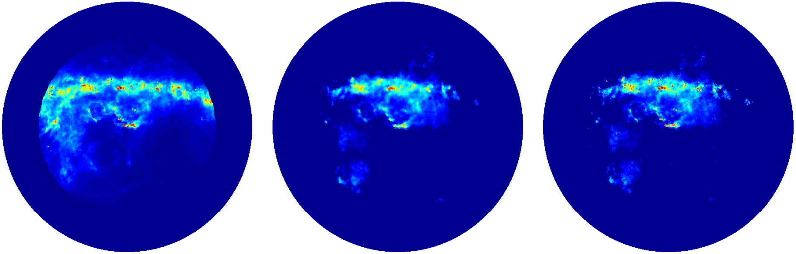

(a) Ground truth (b) Plane ($\text{SNR}_\text{s} = 2.5$dB) (c) Sphere ($\text{SNR}_\text{s} = 2.7$dB)

Figure: BP reconstruction with no chirp.

# Reconstruction of Galactic dust map

- Consider more realistic simulation of 94GHz FDS map of predicted submillimeter and microwave emission of diffuse interstellar Galactic dust [1]
  (available form LAMBDA website: `http://lambda.gsfc.nasa.gov`).
- Downsample to resolution of $N_{\text{side}} = 128$ and consider region of $\theta_{\text{FOV}} = 90^\circ$ centered on Galactic coordinates $(l, b) = (210^\circ, -20^\circ)$.
- Reconstruct from simulated visibilities with 25% coverage.

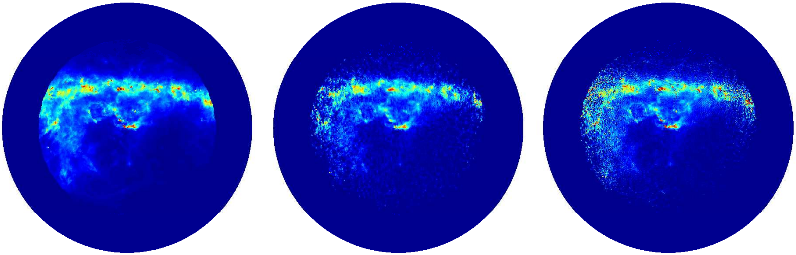

(a) Ground truth (b) Plane ($\text{SNR}_\text{s} = 5.3\text{dB}$) (c) Sphere ($\text{SNR}_\text{s} = 5.0\text{dB}$)

Figure: BP reconstruction with chirp.

# Reconstruction of Galactic dust map

- Consider more realistic simulation of 94GHz FDS map of predicted submillimeter and microwave emission of diffuse interstellar Galactic dust [1]
  (available form LAMBDA website: `http://lambda.gsfc.nasa.gov`).
- Downsample to resolution of $N_{\text{side}} = 128$ and consider region of $\theta_{\text{FOV}} = 90^\circ$ centered on Galactic coordinates $(l, b) = (210^\circ, -20^\circ)$.
- Reconstruct from simulated visibilities with 25% coverage.

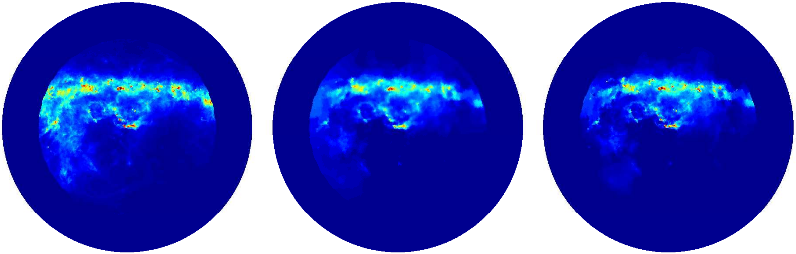

(a) Ground truth (b) Plane ($\text{SNR}_\text{s} = 7.4\text{dB}$) (c) Sphere ($\text{SNR}_\text{s} = 6.7\text{dB}$)

Figure: TV reconstruction with no chirp.

# Reconstruction of Galactic dust map

- Consider more realistic simulation of 94GHz FDS map of predicted submillimeter and microwave emission of diffuse interstellar Galactic dust [1]
  (available form LAMBDA website: `http://lambda.gsfc.nasa.gov`).
- Downsample to resolution of $N_{\text{side}} = 128$ and consider region of $\theta_{\text{FOV}} = 90^\circ$ centered on Galactic coordinates $(l, b) = (210^\circ, -20^\circ)$.
- Reconstruct from simulated visibilities with 25% coverage.

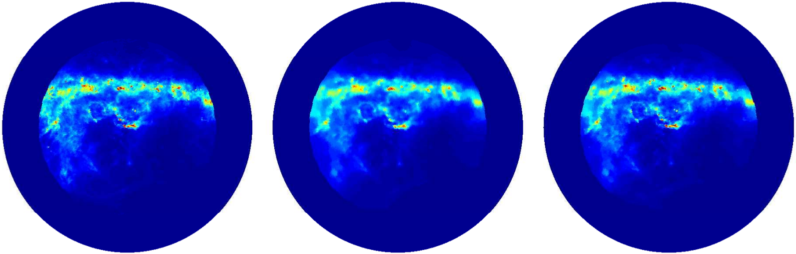

(a) Ground truth (b) Plane ($\text{SNR}_\text{s} = 13.7$dB) (c) Sphere ($\text{SNR}_\text{s} = 19.3$dB)

Figure: TV reconstruction with chirp.

# Summary & future work

- Considered inverse interferometric problem in wide FOV setting, with no small field of view assumptions.
- Chirp modulation more effective due to higher frequency content.
- Signal on the sphere more sparse.
- Coherence on the sphere hampered but mitigated by universality of chirp.
- Quantified performance on Gaussian simulations and illustrated recovery of diffuse interstellar Galactic dust → superiority of sphere.
- Future work:
  - Alternative sparsity bases on the sphere
    (*e.g.* Haar wavelets [4], steerable scale discretised wavelets [5], wavelets on graphs [3])
    → consider analysis problem.
  - Solve inverse problem directly on sphere
    (use fast wavelet method of JDM and Scaife [4] to compute visibilities).

ÉCOLE POLYTECHNIQUE FÉDÉRALE DE LAUSANNE

# Summary & future work

- Considered inverse interferometric problem in wide FOV setting, with no small field of view assumptions.
- Chirp modulation more effective due to higher frequency content.
- Signal on the sphere more sparse.
- Coherence on the sphere hampered but mitigated by universality of chirp.
- Quantified performance on Gaussian simulations and illustrated recovery of diffuse interstellar Galactic dust $\longrightarrow$ superiority of sphere.
- Future work:
    - Alternative sparsity bases on the sphere (*e.g.* Haar wavelets [4], steerable scale discretised wavelets [5], wavelets on graphs [3]) $\longrightarrow$ consider analysis problem.
    - Solve inverse problem directly on sphere (use fast wavelet method of JDM and Scaife [4] to compute visibilities).

# Summary & future work

- Considered inverse interferometric problem in wide FOV setting, with no small field of view assumptions.
- Chirp modulation more effective due to higher frequency content.
- Signal on the sphere more sparse.
- Coherence on the sphere hampered but mitigated by universality of chirp.
- Quantified performance on Gaussian simulations and illustrated recovery of diffuse interstellar Galactic dust $\longrightarrow$ superiority of sphere.
- Future work:
  - Alternative sparsity bases on the sphere
    (*e.g.* Haar wavelets [4], steerable scale discretised wavelets [5], wavelets on graphs [3])
    $\longrightarrow$ consider analysis problem.
  - Solve inverse problem directly on sphere
    (use fast wavelet method of JDM and Scaife [4] to compute visibilities).

# References


[1] D. P. Finkbeiner, M. Davis, and D. J. Schlegel.
Extrapolation of Galactic Dust Emission at 100 Microns to Cosmic Microwave Background Radiation Frequencies Using FIRAS.
*Astrophys. J.*, 524:867–886, October 1999.

[2] K. M. Górski, E. Hivon, A. J. Banday, B. D. Wandelt, F. K. Hansen, M. Reinecke, and M. Bartelmann.
Healpix – a framework for high resolution discretization and fast analysis of data distributed on the sphere.
*Astrophys. J.*, 622:759–771, 2005.

[3] D. K. Hammond, P. Vandergheynst, and R. Gribonval.
Wavelets on graphs via spectral graph theory.
*Applied Comput. Harm. Anal.*, in press, 2010.

[4] J. D. McEwen and A. M. M. Scaife.
Simulating full-sky interferometric observations.
*Mon. Not. Roy. Astron. Soc.*, 389(3):1163–1178, 2008.

[5] Y. Wiaux, J. D. McEwen, P. Vandergheynst, and O. Blanc.
Exact reconstruction with directional wavelets on the sphere.
*Mon. Not. Roy. Astron. Soc.*, 388(2):770–788, 2008.

[6] Y. Wiaux, G. Puy, Y. Boursier, and P. Vandergheynst.
Spread spectrum for imaging techniques in radio interferometry.
*Mon. Not. Roy. Astron. Soc.*, 400:1029–1038, 2009.